RAA 2020 Vol. **20** No. **6**, 98(12pp) doi: 10.1088/1674–4527/20/6/98
© 2020 National Astronomical Observatories, CAS and IOP Publishing Ltd.
http://www.raa-journal.org *http://iopscience.iop.org/raa*

Research in
Astronomy and
Astrophysics

Detection of thermonuclear X-ray bursts and dips from the X-ray binary 4U 1323-62 with *AstroSat*/LAXPC

Yashpal Bhulla[1], Jayashree Roy[2] and S.N.A. Jaaffrey[1]

[1] Pacific Academy of Higher Education and Research University, Udaipur-313003, India; *yash.pkn@gmail.com*
[2] Inter-University Center for Astronomy and Astrophysics, Pune-411007, India

Received 2019 August 4; accepted 2020 January 10

Abstract Using data from the Large Area X-ray Proportional Counter (LAXPC) on the *AstroSat* satellite, we observed Type-1 thermonuclear X-ray bursts from the low mass X-ray binary neutron star 4U 1323–62. Observations of 4U 1323-62 that were carried out during the performance verification phase of the *AstroSat* satellite indicated six thermonuclear X-ray bursts in a total effective exposure of ∼49.5 ks for about two consecutive days. Recurrence time of the detected thermonuclear bursts is in accordance with the orbital period of the source, ∼9400 s. Moreover, the light curve of 4U 1323–62 revealed the presence of two dips. We present the results from time-resolved spectroscopy performed during all of the six X-ray bursts and also report the detection of a known low frequency quasi-periodic oscillation (LFQPO) at ∼1 Hz from the source. However, any evidence of kilohertz QPO was not found. We have shown the burst profile at different energy ranges. Assuming a distance of 10 kpc, we observed a mean flux of $\sim 1.8\times 10^{-9}$ erg cm^2 s^{-1}. The radius of the blackbody is found to be highly consistent with the blackbody temperature and the blackbody flux of the bursts.

Key words: accretion — accretion disc — stars: neutron star — X-rays: binaries — X-rays: thermonuclear bursts — individual: 4U 1323–62

1 INTRODUCTION

Low mass X-ray binaries (LMXBs) are systems in which the compact object, a neutron star (NS) or a black hole (BH), accretes matter from the companion star via Roche lobe overflow (Hasinger & van der Klis 1989; Urpin et al. 1998; van der Klis 2006; Reig 2011; Belloni & Stella 2014; Motta 2016; Chauhan et al. 2017; Bhulla et al. 2019). In LMXBs, a number of periodic and quasi-periodic oscillations (QPOs) have been observed (Méndez & van der Klis 1999; van der Klis 2000; Méndez 2000; Méndez et al. 2001; Barret et al. 2005). These QPOs are attributed to instabilities in the accretion disk. (Homan et al. 2005; Ingram & Done 2011; Scaringi 2015). LMXBs span a broad range of luminosities from $\sim 10^{36}$ to a few times 10^{38} erg s^{-1} (Church et al. 2014; Wang 2016). Weakly magnetized and luminous NS LMXBs are classified into Z and atoll sources based on their color-color diagram (CCD) and hardness intensity diagram (HID) (Hasinger & van der Klis 1989; Mondal et al. 2018).

It has been observed in some NS sources that the X-ray luminosity increases by a factor of ∼10 in about a few seconds, approaching the Eddington luminosity $L_{\rm Edd} =\sim 10^{38}$ ergs s^{-1} band, then fades with a timescale of ∼10 s. This phenomenon is known as thermonuclear type-I X-ray bursts (Strohmayer & Bildsten 2006; Galloway et al. 2008). The first type-I X-ray burst was discovered in the 1970s. The Multi-INstrument Burst ARchive (MINBAR)[1] is a database containing the analysis of more than 7000 type-I thermonuclear X-ray bursts from 84 burst sources, that are observed by different X-rays observatories including *BeppoSAX*, *Rossi X-ray Timing Explorer (RXTE)* and *INTEGRAL*. Type-I X-ray bursts are flashes due to the unstable thermonuclear burning of accreted and accumulated material on an NS (Grindlay et al. 1976; Belian et al. 1976; Bildsten 1998; Strohmayer & Bildsten 2006; Galloway & Keek 2017a; Beri et al. 2019). This ignition condition is caused due to a hydrogen and/or helium enriched component supplied by a companion star to trigger the burning (Hansen & van Horn 1975; Woosley & Taam 1976; Maraschi & Cavaliere 1977; Lamb & Lamb 1978; Lewin et al. 1993; Strohmayer & Bildsten 2006). Bursts generally appear as short transient events where the X-ray intensity increases rapidly on a timescale of a few seconds and decays in an exponential trend back to the pre-burst level. The decay time is always more than the rise time and the du-

---

[1] `http://burst.sci.monash.edu/minbar/`

ration of a thermonuclear burst ranges from a few seconds to half an hour. The time interval of burst-to-burst events is typically on the order of hours to days. The time interval is supposed to accumulate enough fuel to generate another burst. After the X-ray eruptions, luminosity recedes to its pre-burst stage (Lewin & van den Heuvel 1984; Tawara et al. 1984).

Thermonuclear X-ray bursts have been studied with the *RXTE*/Proportional Counter Array (*RXTE*/PCA) (Galloway et al. 2003, 2004). The shortest recurrence time for NS 4U 1636–536 is ∼5.4 min as reported by Linares et al. (2009) by analyzing *RXTE*/PCA observations. Keek et al. (2010) observed the shortest recurrence time from 4U 1705–44 to be ∼3.8 min. MINBAR located the 61 X-ray burst sources by *RXTE*/PCA, 56 burst sources by *BeppoSAX* and 62 X-ray burst sources observed by *INTEGRAL*.

The energy spectra of thermonuclear bursts consist of emissions from the NS surface or boundary layer (Hanawa 1989; Popham & Sunyaev 2001; Gilfanov et al. 2003a). Thermonuclear bursts can occur in two different spectral states, namely low/hard (island state) and high/soft (banana state) spectral states in the CCD. The characteristics of these thermonuclear bursts are unique in both the states. (Galloway et al. 2008). The different spectral states are thought to originate from different accretion processes. Thermal instability triggers the viscous instability, and as the temperature increases, the mass accretion rate also increases (Done et al. 2007). During the rising part of the burst, observed energy spectra are generally hard, whereas the spectrum becomes soft during the decay phase of the thermonuclear burst (Zhang et al. 2011; Degenaar et al. 2018). In the high/soft state, the disk approaches the NS surface and terminates emission from the boundary layer (Mitsuda et al. 1984; Gilfanov et al. 2003b). The disk is assumed to be geometrically thin and optically thick close to the central object. However, in the low/hard state, the innermost accretion occurs through an optically thin, truncated disk and the emission from the source may originate from the hot corona (Ubertini et al. 1999; Done et al. 2007; Degenaar et al. 2016; Galloway & Keek 2017b; Bhattacharyya et al. 2018).

The energy spectrum of the thermonuclear burst sources is fit well by a sum of blackbody components with interstellar absorption and a thermal Comptonization model. The blackbody component originates due to emission from the innermost part of the accretion disk and the NS surface (Swank et al. 1977; Keek et al. 2014a; Degenaar et al. 2016; Galloway & Keek 2017a). The measured blackbody temperature of X-ray bursts, $kT_{bb} \approx 1 - 3\,\mathrm{keV}$, evolves with time (Done et al. 2007; Galloway & Keek 2017b). Moreover, several recent studies described the absorption and emission features observed during the X-ray bursts which might indicate a mass point outflow or change in the accretion disk (Ballantyne & Strohmayer 2004; Ballantyne & Everett 2005; Keek et al. 2014b; Galloway & Keek 2017a). The luminosity and exposure of a burst depend on the mass accretion rate and chemical composition of the accreted material. At the peak, the burst emission may exceed the Eddington limit $L_{\mathrm{Edd}} \approx 2 \times 10^{38}\,\mathrm{erg\,s^{-1}}$ (Lewin et al. 1993). During the expansion phase of the burst, the luminosity may reach or exceed the Eddington limit locally at the surface, resulting in photospheric expansion. The photosphere regains its original size after the thermonuclear burning (rp-process) of the H/He mixture ceases and finally the star cools down to roughly constant radius (Lewin et al. 1993; Ballantyne & Strohmayer 2004; Boutloukos et al. 2010; Degenaar et al. 2016; Galloway & Keek 2017b).

4U 1323–62 is a faint LMXB source, which was first detected by *Uhuru* and *Ariel V* (Forman et al. 1978; Warwick et al. 1981). The source exhibits regular thermonuclear type-1 X-ray bursts, and periodic intensity dips were first discovered by *EXOSAT* observations from 1985 February $11 - 13$ (van der Klis et al. 1985; Parmar et al. 1989; Gambino et al. 2016). MINBAR is utilized to locate the *RXTE*/PCA observations of 4U 1323–62 that manifested 40 bursts with a recurrence time of $2.45 - 2.59$ hr. From the characteristics of the bursts, the distance to the source was constrained to $10 - 20$ kpc (Parmar et al. 1989). Frank (1987) suggested that the existence of periodic dips indicates the presence of a high inclination angle $\angle i = 60^\circ - 80^\circ$, where $\angle i$ is the angle between the line of sight and the rotation axis of the accretion disk. The source is located at 0.5° above the Galactic plane and shows a prominent dust halo (Barnard et al. 2001). The well defined spectrum of this source was described by *BeppoSAX* and *RXTE*/PCA observations (Bałucińska-Church et al. 1999, 2009). In the *RXTE*/PCA observation, the author reports the presence of an Fe emission feature at 6.43 keV with a width of 1.1 keV. In April 1997, a QPO was discovered at ∼1 Hz (Balman 2010). The QPO was detected in this source during the bursts, dips and as well as during persistent emission (Jonker et al. 1999; Homan et al. 1999).

In this work, we present the detailed temporal and spectral study of the six thermonuclear bursts and two dips observed during *AstroSat*/Large Area X-ray Proportional Counter (LAXPC) observation (Table 1). We examine energy dependent burst profiles and time resolved spectroscopy of the source.

2 OBSERVATIONS AND DATA REDUCTION

AstroSat is the first Indian multiwavelength space astronomy observatory, launched on 2015 September 28. There are five instruments (Scanning Sky Monitor (SSM), Soft X-ray Telescope (SXT), Large Area X-ray Proportional Counter (LAXPC), Cadmium Zinc Telluride Imager

Table 1 The observation logs of 4U 1323–62 data by different instruments that detect the orbit period. * represents the detection of one doublet and ** signifies the two doublets identified in the light curve.

Instrument	Obs. Time	Exposure (ks)	Bursts	Dips	Orbital Period	Reference
EXOSAT/ME	1985 February 11 – 13	108	6	10	2.932 hr	Parmar et al. (1989)
RXTE/PCA	1997 April 25 – 28	200	7**	7	2.45 – 2.59 hr	Barnard et al. (2001)
BeppoSAX/MECS	1997 August 22 & 24	120	10	12	2.40 – 2.57 hr	Bałucińska-Church et al. (2009)
XMM-Newton	2003 January 29	50	7	5	2.97 hr	Church et al. (2005)
RXTE/PCA	2003 September 25	200	7	4	2.45 – 2.59 hr	Gambino et al. (2016)
SUZAKU	2007 January 9 – 10	122.5	5*	11	2.926 hr	Bałucińska-Church et al. (2009)
CHANDRA	2011 December 19	60	9	6	2.94 hr	Gambino et al. (2016)
CHANDRA	2011 December 23	80	13*	8	2.94 hr	Gambino et al. (2016)
LAXPC	2017 February 16 – 17	49.5	6	2	∼2.66 hr	present

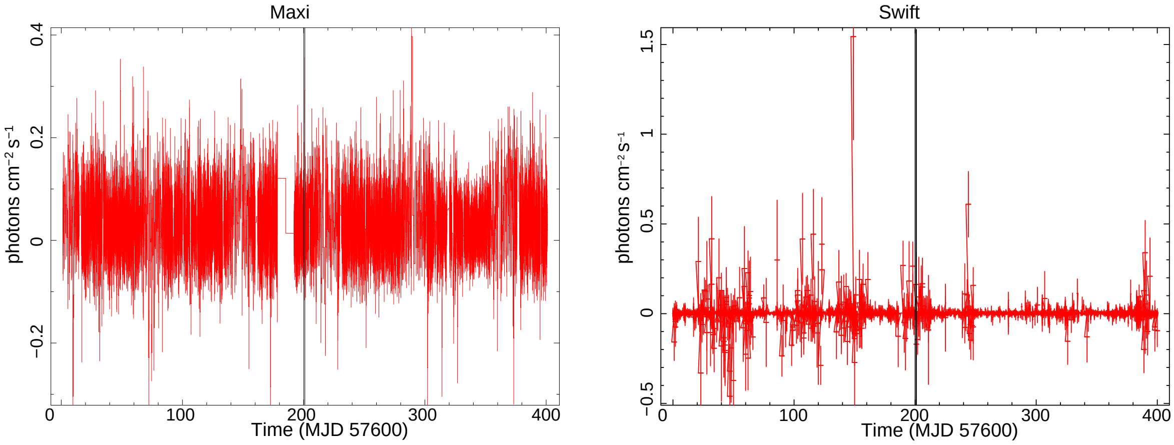

Fig. 1 These figures indicate variability in the light curve of the 4U 1323–62 NS by considering the MAXI light curve in the 2 – 20 keV range in the *left* panel and *Swift*/BAT light curve in the 15 – 50 keV range in the *right* panel. The *bold line* in both figures highlights the LAXPC observation time (i.e., MJD: 57800-57801).

(CZTI) and Ultraviolet Imaging Telescope (UVIT)) onboard *AstroSat* which cover a wide energy range (Agrawal 2006; Paul 2013; Yadav et al. 2016b; Roy et al. 2016). LAXPC is one of the major instruments onboard the *AstroSat* satellite. The LAXPC instrument is providing high time resolution X-ray data in the 3 – 80 keV energy range. *AstroSat* consists of a set of three co-aligned identical LAXPC detectors to provide total effective area of ∼6000 cm^2 at 15 keV (Antia et al. 2017). The three LAXPC units are named LAXPC-10, LAXPC-20 and LAXPC-30. The energy resolutions of LAXPC units are 20% and 10% at 6 and 60 keV respectively (Yadav et al. 2016a). LAXPCs are a multi-anode and multi-layer configuration having a field of view of about $1^\circ \times 1^\circ$. Each LAXPC unit has five layers consisting of 12 detector cells. Each LAXPC independently observes the source (Yadav et al. 2016b; Agrawal et al. 2017; Antia et al. 2017).

The data were collected by LAXPCs in two different modes: Event Analysis mode (modeEA) and Broad Band Counting (modeBB). Event mode data give information about the energy of each photon and its arrival time at 10 ms accuracy. We have used event analysis mode modeEA data for generating the light curves, power density spectrum (PDS) and energy spectrum of the source. Due to the wide energy range and large photon collecting area, *AstroSat* efficiently observes thermonuclear X-ray burst sources. The source 4U 1323–62 was observed by *AstroSat*/LAXPC from 2017 February 16 05:25:43 till 2017 February 17 08:35:35 for a total effective exposure time of 49.5 ks. The LAXPC data were downloaded from the ASSC astrobrowser[2].

3 DATA ANALYSIS AND RESULTS

The data are analyzed using the individual routine LaxpcSoft[3] to obtain background subtracted light curves and energy spectra (Antia et al. 2017). The commands are applied to extract the light curve, and the associated spectral files are $laxpc\_make\_lightcurve$ and $laxpc\_make\_spectra$. The background files for light curve and spectra are extracted by inputting the commands $laxpc\_make\_backlightcurve$ and $laxpc\_make\_backspectra$. The data analysis was done by HEASOFT 6.19[4], which consists mainly of FTOOLS[5],

---

[2] `https://astrobrowse.issdc.gov.in/astro_archive/archive`

[3] `http://AstroSat-ssc.iucaa.in/?q=laxpcData`

[4] `http://heasarc.nasa.gov/ftools`

[5] `https://heasarc.gsfc.nasa.gov/ftools`

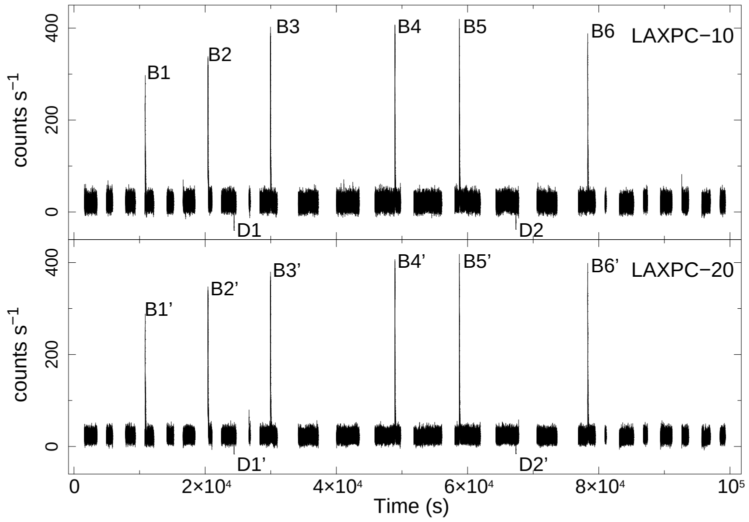

Fig. 2 Background subtracted light curve in the $3-20$ keV energy range using LAXPC-10 and LAXPC-20 data of 4U 1323–62. The light curve is binned with a bin size of 1 s. Multiple bursts and dips have been displayed in this figure. In the *upper* panel of the plot, B and D stand for burst and dip respectively with consecutive numbers for LAXPC-10. B' and D' are the labels for burst and dip observed by LAXPC 20 respectively.

Table 2 The X-ray bursts and dips, rise and decay time interval along with wait time observed utilizing LAXPC 10 and LAXPC 20 are tabulated.

			LAXPC-10			
Burst	Start-End Time	Rise Time (t') (s)	Decay Time (t'') (s)	Burst Exposure (s)	Wait Time (hr)	Peak Intensity (count s^{-1})
B1	10856–10931	13	62	75	-	295
B2	20423–20513	6	84	90	2.636	318
B3	29962–30056	8	86	94	2.625	382
B4	48914–49015	11	90	101	—–	388
B5	58737–58830	10	83	93	2.70	399
B6	78312–78410	11	87	98	—–	368
Dip	Start-End Time	Rise Time (t') (s)	Decay Time (t'') (s)	Burst Exposure (s)	Wait Time (hr)	
D1	24416–24421	3	2	5	—	
D2	67366–67370	2	2	4	11.928	
			LAXPC-20			
Burst	Start-End Time	Rise Time (t') (s)	Decay Time (t'') (s)	Burst Exposure (s)	Wait Time (hr)	Peak Intensity (count s^{-1})
B1'	10857–10932.5	13	62.5	75.5	-	289
B2'	20423–20512	7	82	89	2.636	328
B3'	29962–30057	9	86	95	2.625	367
B4'	48914–49013	11	88	99	—–	390
B5'	58737–58829	9	83	92	2.70	398
B6'	78312–78411	12	87	99	—–	378
Dip	Start-End Time	Rise Time (t') (s)	Decay Time (t'') (s)	Burst Exposure (s)	Wait Time (hr)	
D1'	24416.5–24419	1	2	3	—	
D2'	67366–67370	2	2	4	11.928	

XORONOS and XSPEC (Arnaud 1996; Noble & Nowak 2008). We observed that the thermonuclear bursts and dips in the light curve are present in both LAXPC units (LAXPC 10 and 20) as displayed in Figure 2. For generating the light curves and spectral analysis, we only considered data from the top layer of LAXPC-10 and LAXPC-20. The top layer of the LAXPC detector absorbs 90% of the X-ray photons below 20 keV (Roy et al. 2016). We have not applied data from LAXPC-30 for this work due to gain instability caused by gas leakage as suggested by Antia et al. (2017).

The results of previously reported thermonuclear bursts and dips observed from the source from various missions are presented in Table 1. This table indicates the reports of orbital period estimates based on the recurrence time of the thermonuclear bursts. The light curves of each burst and dip from both LAXPC detectors are plotted in Figures 3 and 4 respectively, where the horizontal and ver-

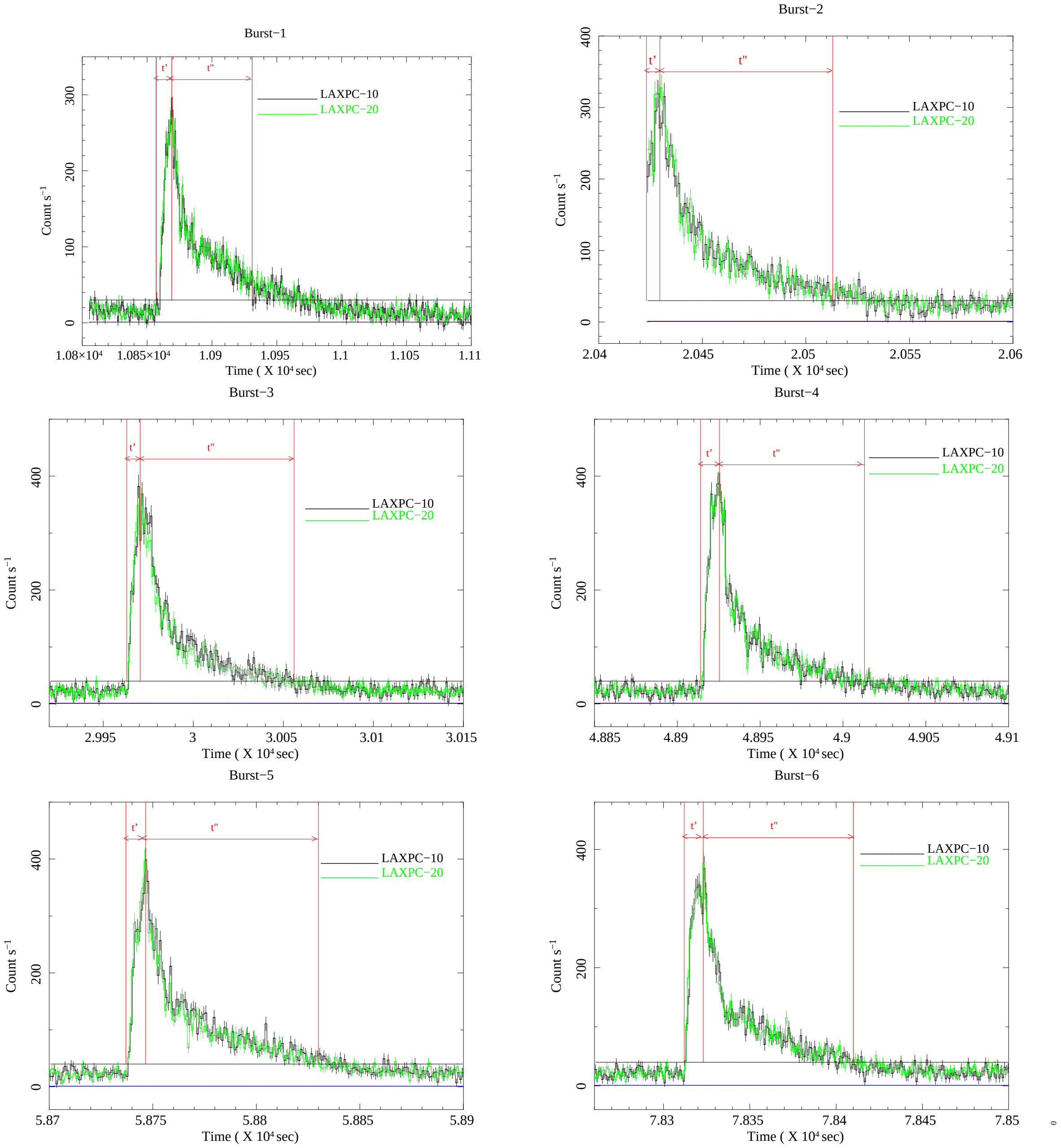

Burst−1 Burst−2 Burst−3 Burst−4 Burst−5 Burst−6

Fig. 3 The panels display the bursts and dips in the $3-20\,\mathrm{keV}$ energy range using LAXPC-10 (*black*) and LAXPC-20 (*green*) observations in a 1 s binned light curve.

tical lines indicate the rise (t') and decay (t'') times of the bursts.

3.1 Light Curves

We used the orbit binned light curve of the MAXI[6] transient monitor in the soft energy band ($3-20\,\mathrm{keV}$) and the *Swift*/BAT Transient Monitor (Krimm et al. 2013) light curve in the hard energy band ($15-50\,\mathrm{keV}$) of 4U 1323–62 to determine the spectral state of this source. In both instruments, the light curve of 4U 1323–62 manifests long-term variability in intensity from 2016 July 31 to 2017 September 4. The bold line in both panels of Figure 1 highlights the LAXPC observation time of 4U 1323–62. In Figure 2, LAXPC-10 and LAXPC-20 observations of 4U 1323–62 show the light curve in the $3-20\,\mathrm{keV}$ energy range binned with a bin size of 1 s. In light curve data, gaps and thermonuclear X-ray bursts are detected.

During the 100 ks observation of the *AstroSat*/LAXPC observation of the source, six thermonuclear bursts were observed as depicted in Figure 2. We adopt the nomenclature of B1, B2, B3, B4, B5 and B6 to indicate the ther-

---

[6] `http://maxi.riken.jp/star_data/J1326-621/J1326-621.html`

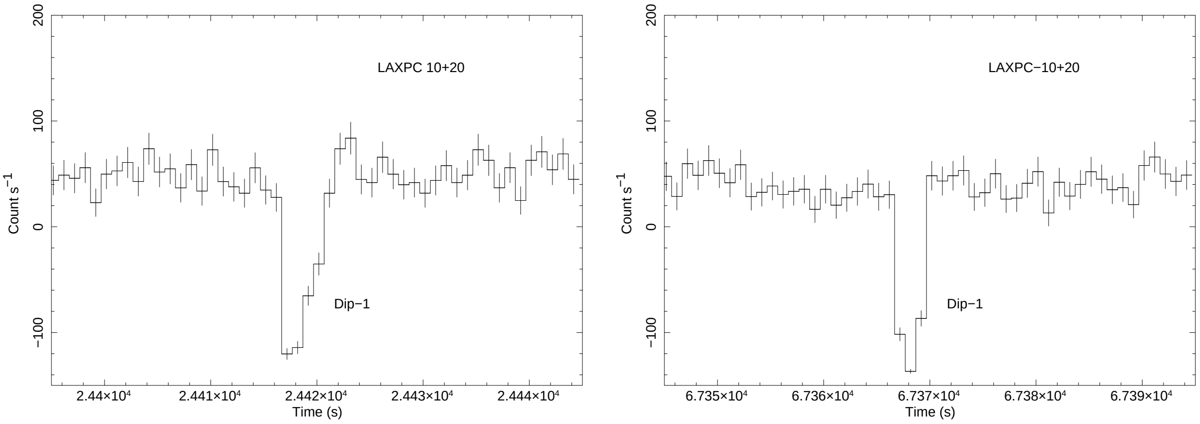

Fig. 4 The figures display the dips in the $3-20\,\mathrm{keV}$ energy range using merged LAXPC-10 and LAXPC-20 observations in a 1 s binned light curve.

Table 3 This table lists the maximum count rate, and the rise and decay times of the fifth thermonuclear X-ray burst in different energy bands.

Energy (keV)	Peak-count (count s^{-1})	Burst-rising (s)	Burst-decay (s)
$3 - -6.2$	140	9.5	84.5
$6.2 - -9$	119	10	85.5
$9 - -12$	72	10	91
$12 - -16$	47	10.5	96
$16 - -20$	24	18	22

monuclear bursts in the LAXPC 10 light curve and B1’, B2’, B3’, B4’, B5’ and B6’ in the LAXPC 20 light curve. We observed that there is a gap between the successive bursts, B3 and B4 and the bursts B5 to B6 are twice the wait time observed during the consecutive bursts B1 and B2. These missed bursts are attributed to data gaps. The data gaps, during the occurrence of bursts, are due to the position of the satellite over the South Atlantic Anomaly (SAA) region.

Each burst has an exposure time (rise and decay time) between $75-100\,\mathrm{s}$ and a high peak count rate of $\approx$380 count s^{-1}, as plotted in the light curve (Fig. 3). In Table 2, the burst rise and decay time interval, exposure of each burst, wait time and peak count rate have been tabulated. In Figure 4, prominent dips are evident in the $3-20\,\mathrm{keV}$ energy range using observations of both of LAXPC units (LAXPC 10 and LAXPC 20).

3.2 Energy-Resolved Burst Profiles

To probe the thermonuclear X-ray burst in different energy bands, we generated 1 s binned light curves from LAXPC 10 and 20 during X-ray bursts in six different narrow energy bands: $3-6.2\,\mathrm{keV}$, $6.2-9\,\mathrm{keV}$, $9-12\,\mathrm{keV}$, $12-16\,\mathrm{keV}$, $16-20\,\mathrm{keV}$ and $20-80\,\mathrm{keV}$. The light curves were generated from only the top layer of LAXPC 10 and LAXPC 20. Figure 5 displays the energy resolved light curve of the fifth burst (B5) seen in the observation of 4U 1323–62. The energy dependent thermonuclear burst profile clearly demonstrates that the decay time decreases with the increase in energy.

As per Table 3, the maximum intensity is accumulated at the low energy range ($3-6.2\,\mathrm{keV}$). For the soft energy region, the rise time is relatively short. However, in the energy range from $16-20\,\mathrm{keV}$, the peak intensity is lowest, and the rise time took the maximum time to reach a peak intensity level and in the $20-80\,\mathrm{keV}$ energy range, the thermonuclear burst is absent. It may be inferred from Figure 5 and Table 3 that 4U 1323–62 was observed in a soft spectral state during the *AstroSat*/LAXPC observations.

We measured the energy dependence of the burst duration in all six X-ray bursts. We found that there was a gradual decay in the intensity with an increase in energy. The rise and decay time for all the bursts have been tabulated in Table 2.

3.3 Power Density Spectra

In the persistent emission, PDS was computed in the $3-20\,\mathrm{keV}$ energy band. The light curve extracted from LAXPC-10 and 20 was applied to generate PDS utilizing the ‘FTOOLS’ task “Powspec.” The Poissonian noise level is subtracted from each power spectrum. PDS was Leahy normalized ($(\mathrm{rms/mean})^2\,\mathrm{Hz}^{-1}$), such that the integration of the power spectra gave the fractional root mean square (rms) variation.

A clear QPO was detected in the power spectra during the bursts. The QPO was fitted by employing a Lorentzian model. We have observed the low frequency QPO (LFQPO) of $\sim$1 Hz, which was reported by Balman (2010) using *RXTE*/PCA data. To detect the LFQPO, we considered a light curve binned with a bin size of 0.01 s. The light curve was divided into each segment with 2048 bins. Figure 6 displays the QPO detected during the thermonuclear burst. The observed $\sim$3 sigma significant QPO

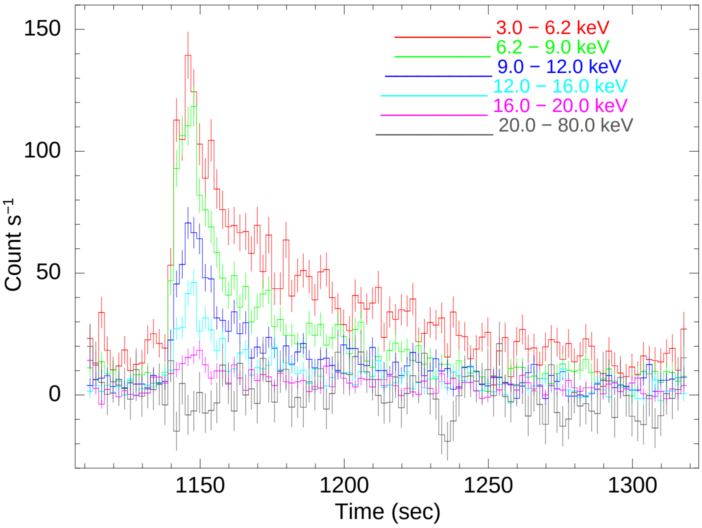

Fig. 5 This plot shows a light curve of the fifth thermonuclear X-ray burst in different energy bands. The softest energy range ($3 - 6.2$ keV) has the highest count rate.

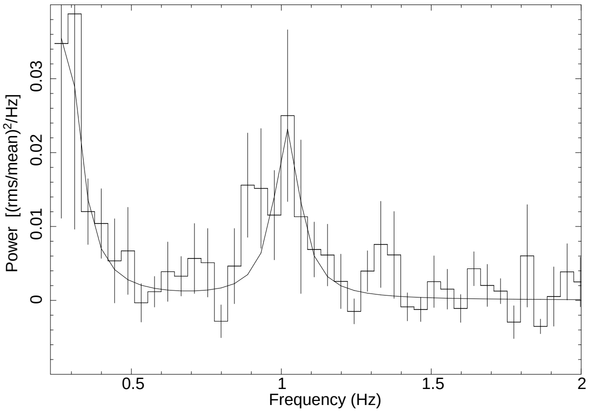

Fig. 6 PDS generated from 0.01 s binned light curve by merging LAXPC 10 and 20, which manifest low frequency ~1 Hz QPO in the $3 - 20$ keV energy range.

frequency is 0.97 Hz. The rms of the QPO=6.7% and the quality factor is ~18. Jonker et al. (1999) previously discovered an LFQPO at a $0.77 - 0.87$ Hz QPO from the source 4U 1323–62 using *RXTE*/PCA data. The amplitude of the QPO detected from the source was found to be constant during the persistent emission and X-ray dips during the type-1 X-ray thermonuclear bursts (Jonker et al. 1999).

3.4 Energy Spectra: Time Resolved Spectroscopy

Spectral fitting for individual X-ray bursts was carried out. To investigate the spectral evolution during X-ray bursts, we performed time-resolved spectroscopy on each type-1 thermonuclear burst. Therefore, the burst data were divided into segments of 10 s intervals. Each burst has $8 - 12$ segments. These 10 s data segments during each burst are used to reveal the evolution of the blackbody component in energy spectra. For each burst except the second burst (B2), we extracted the spectra for 10 s of data preceding the bursts. In burst B2, we have extracted the spectra from data after the burst decayed completely to the persistent levels. There was no difference in the distributions of best-fitting persistent models between the pre- and post-bursts. The spectra extracted from persistent emission was utilized to subtract for all burst segments as the background.

To study the variation of NS radii and flux during the burst, the contribution from the persistent emission spectrum component is excluded. Decoupling the burst component of the spectrum from the persistent part was difficult, as the various components were usually spectrally degenerated.

To generate energy spectra during the persistent emission pre-burst phase, we selected a 10 s stretch of data prior to the thermonuclear burst. To fit the energy spectrum, different model combinations (available in XSPEC) were applied: (i) tbabs (bbodyrad+powerlaw), (ii) tbabs (bbodyrad+diskbb), (iii) tbabs (bbodyrad+powerlaw+gaussion), (iv) tbabs (nthcomp+gaussion) and (v) tbabs (nthcomp). We observed that the model [tbabs*(nthcomp)] is the best fit (lowest reduced χ^2) to the persistent energy spectrum in the $2 - 20$ keV energy range. The hydrogen column density is fixed at $N_H = 4 \times 10^{22}$ cm^2 (Boirin et al. 2005).

The burst energy spectra in the $3 - 20$ keV energy band were fitted with the standard approach: a blackbody model consisting of two parameters, a temperature (kT_{bb}) and normalization along with the persistent emission component of the corresponding burst. The parameters of the persistent emission component were frozen during the burst spectra. These spectral components took into account the

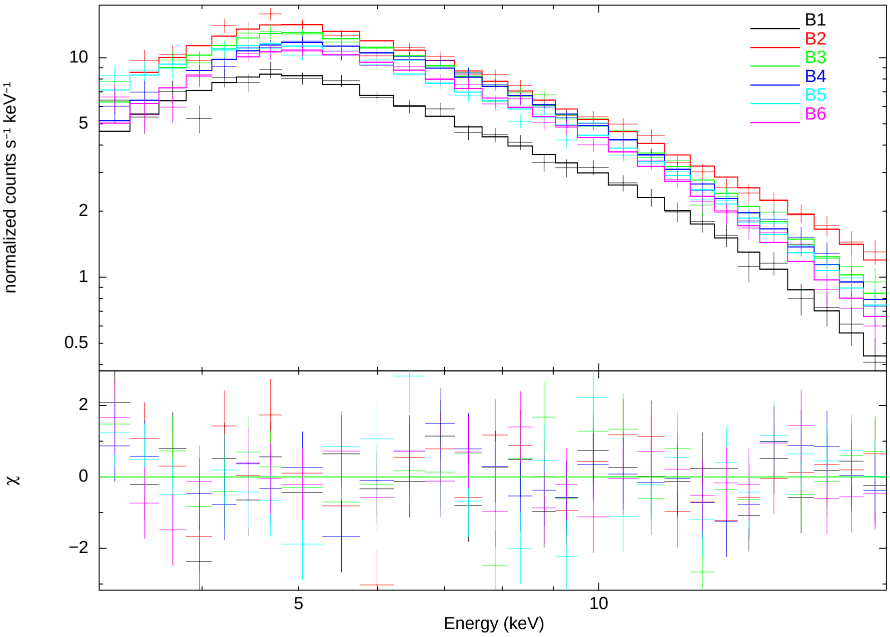

Fig. 7 The energy spectra of the six thermonuclear X-ray bursts observed by LAXPC 10 in the $3-20$ keV energy range is depicted in this figure.

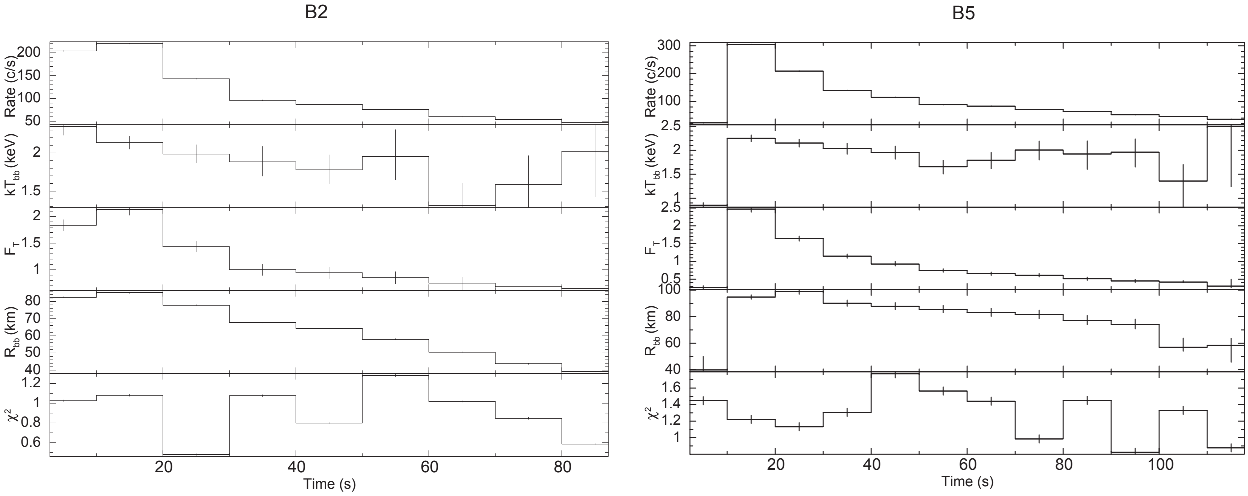

Fig. 8 The best fit parameters obtained by performing time resolved spectroscopy on two of the observed bursts (B2 and B5) in the LAXPC-10 observation. The top panel depicts the average count rate (without error) for each segment.

nature of the seed photons (represented by the inp-type parameter that is equal to 0 for blackbody seed photons). This approach was implemented to understand the evolution in blackbody parameters. The assumed blackbody emission describes the burst spectra well from the surface of the NS and Comptonization emission from the extended accretion disk corona (ADC) (Balucińska-Church et al. 2001; Church et al. 2002).

The unabsorbed bolometric flux (in the range $3-80$ keV) was computed using the XSPEC function “cflux.” The total flux varies uniformly. The blackbody radius also varies consistently and shows a positive Pearson correlation with kT_{bb}. R_{bb} is the blackbody radius and d_{10} is the source distance in units of 10 kpc. $R_{bb} = [N \times (\mathrm{distance})^2/4\pi\mathrm{flux}]^{1/2}$ is obtained at the minimum distance of the source at 10 kpc.

The emission radii were estimated from the blackbody normalization. All the observed fit parameters have been depicted in multi-panel plots with incremental time segments for each of the six bursts, as shown in Figure 8. The first panel of each figure displays the variation in count rate during the burst. The second panel shows the evolution of

Table 4 Fitting results of bursts $1-3$ from observations of 4U 1323–62. Here we provide the total unabsorbed flux from $0.001-100$ keV in the unit erg cm^2 s^{-1}.

LAXPC-10

Burst-1

Segment	Rate (count s^{-1})	kT_{in} (keV)	Flux × 10^{-9}	Radius (km)	Chi-square
5^{+5}_{-5}	15^{+1}_{-1}	$3.05^{+0.27}_{-0.32}$	$0.11^{+0.035}_{-0.050}$	$74.31^{+5.94}_{-5.94}$	$1.074^{+0.05}_{-0.05}$
15^{+5}_{-5}	183^{+1}_{-1}	$2.19^{0.092}_{-0.096}$	$1.47^{+0.067}_{-0.068}$	$95.62^{+2.42}_{-2.15}$	$0.91^{+0.05}_{-0.05}$
25^{+5}_{-5}	179^{+1}_{-1}	$2.07^{+0.090}_{-0.094}$	$1.48^{+0.056}_{-0.076}$	$96.00^{+2.21}_{-2.25}$	$1.34^{+0.05}_{-0.05}$
35^{+5}_{-5}	109^{+1}_{-1}	$1.89^{+0.11}_{-0.12}$	$0.81^{+0.05}_{-0.05}$	$93.82^{+3.03}_{-2.12}$	$1.73^{+0.05}_{-0.05}$
45^{+5}_{-5}	98^{+1}_{-1}	$1.79^{+0.11}_{-0.12}$	$0.74^{+0.048}_{-0.048}$	$93.56^{+3.16}_{-2.44}$	$1.08^{+0.05}_{-0.05}$
55^{+5}_{-5}	82^{+1}_{-1}	$1.76^{+0.14}_{-0.16}$	$0.62^{+0.044}_{-0.045}$	$92.32^{+3.48}_{-3.05}$	$1.18^{+0.05}_{-0.05}$
65^{+5}_{-5}	68^{+1}_{-1}	$1.75^{+0.16}_{-0.18}$	$0.53^{+0.042}_{-0.042}$	$90.87^{+3.87}_{-4.22}$	$0.92^{+0.05}_{-0.05}$
75^{+5}_{-5}	61^{+1}_{-1}	$1.7^{+0.19}_{-0.22}$	$0.41^{+0.039}_{-0.039}$	$88.37^{+4.46}_{-4.39}$	$1.97^{+0.05}_{-0.05}$
85^{+5}_{-5}	41^{+1}_{-1}	$1.44^{+0.20}_{-0.24}$	$0.31^{+0.036}_{-0.037}$	$85.19^{+5.46}_{-3.09}$	$1.21^{+0.05}_{-0.05}$
95^{+5}_{-5}	43^{+1}_{-1}	$1.24^{+0.25}_{-0.30}$	$0.50^{+0.06}_{-0.036}$	$67.74^{+5.02}_{-3.8}$	$1.68^{+0.05}_{-0.05}$
105^{+5}_{-5}	42^{+1}_{-1}	$1.55^{+0.26}_{-0.31}$	$0.29^{+0.035}_{-0.035}$	$83.57^{+5.47}_{-4.77}$	$0.95^{+0.05}_{-0.05}$

Burst-2

Segment	Rate (count s^{-1})	kT_{in} (keV)	Flux × 10^{-9}	Radius (km)	Chi-square
5^{+5}_{-5}	204^{+1}_{-1}	$2.34^{+0.11}_{-0.11}$	$1.83^{+0.10}_{-0.10}$	$82.44^{+0.43}_{-0.37}$	$1.02^{+0.01}_{-0.01}$
15^{+5}_{-5}	220^{+1}_{-1}	$2.13^{+0.087}_{-0.084}$	$2.13^{+0.10}_{-0.10}$	$85.20^{+0.37}_{-0.46}$	$1.08^{+0.01}_{-0.01}$
25^{+5}_{-5}	143^{+1}_{-1}	$1.98^{+0.12}_{-0.11}$	$1.43^{+0.10}_{-0.10}$	$77.81^{+0.43}_{-0.34}$	$0.47^{+0.01}_{-0.01}$
35^{+5}_{-5}	96^{+1}_{-1}	$1.88^{+0.20}_{-0.18}$	$1.0^{+0.10}_{-0.10}$	$67.73^{+0.31}_{-0.31}$	$1.07^{+0.01}_{-0.01}$
45^{+5}_{-5}	87^{+1}_{-1}	$1.77^{+0.19}_{-0.18}$	$0.94^{+0.10}_{-0.10}$	$64.30^{+0.33}_{-0.25}$	$0.79^{+0.01}_{-0.01}$
55^{+5}_{-5}	76^{+1}_{-1}	$1.95^{+0.35}_{-0.30}$	$0.85^{+0.11}_{-0.11}$	$57.95^{+0.37}_{-0.38}$	$1.28^{+0.01}_{-0.01}$
65^{+5}_{-5}	60^{+1}_{-1}	$1.31^{+0.29}_{-0.30}$	$0.74^{+0.11}_{-0.15}$	$50.45^{+0.38}_{-0.43}$	$1.02^{+0.01}_{-0.01}$
75^{+5}_{-5}	54^{+1}_{-1}	$1.58^{+0.37}_{-0.48}$	$0.68^{+0.49}_{-0.19}$	$43.75^{+0.31}_{-0.36}$	$0.84^{+0.01}_{-0.01}$
85^{+5}_{-5}	47^{+1}_{-1}	$2.02^{+0.56}_{-0.59}$	$0.64^{+0.46}_{-0.17}$	$39.18^{+0.31}_{-0.37}$	$0.59^{+0.01}_{-0.01}$

Burst-3

Segment	Rate (count s^{-1})	kT_{in} (keV)	Flux × 10^{-9}	Radius (km)	Chi-square
5^{+5}_{-5}	26^{+1}_{-1}	$0.77^{+0.23}_{-0.30}$	$0.23^{+0.052}_{-0.046}$	$75.53^{+6.73}_{-5.15}$	$0.935^{+0.05}_{-0.05}$
15^{+5}_{-5}	317^{+1}_{-1}	$2.24^{+0.070}_{-0.072}$	$2.30^{+0.083}_{-0.083}$	$95.16^{+1.77}_{-1.69}$	$1.33^{+0.05}_{-0.05}$
25^{+5}_{-5}	193^{+1}_{-1}	$2.21^{+0.078}_{-0.081}$	$0.20^{+0.012}_{-0.10}$	$93.85^{+2.62}_{-2.12}$	$1.12^{+0.05}_{-0.05}$
35^{+5}_{-5}	116^{+1}_{-1}	$1.99^{+0.11}_{-0.12}$	$0.10^{+0.11}_{-0.11}$	$91.32^{+2.22}_{-2.7}$	$1.16^{+0.05}_{-0.05}$
45^{+5}_{-5}	102^{+1}_{-1}	$1.79^{+0.12}_{-0.13}$	$0.80^{+0.050}_{-0.050}$	$88.84^{+2.92}_{-2.66}$	$1.098^{+0.05}_{-0.05}$
55^{+5}_{-5}	80^{+1}_{-1}	$1.82^{+0.16}_{-0.18}$	$0.65^{+0.047}_{-0.047}$	$85.90^{+3.27}_{-3.75}$	$1.15^{+0.05}_{-0.05}$
65^{+5}_{-5}	65^{+1}_{-1}	$1.68^{+0.18}_{-0.19}$	$0.49^{+0.043}_{-0.043}$	$81.62^{+3.87}_{-3.05}$	$1.77^{+0.05}_{-0.05}$
75^{+5}_{-5}	62^{+1}_{-1}	$1.64^{+0.20}_{-0.22}$	$0.45^{+0.044}_{-0.038}$	$78.25^{+2.8}_{-3.33}$	$1.11^{+0.05}_{-0.05}$
85^{+5}_{-5}	50^{+1}_{-1}	$1.59^{+0.21}_{-0.25}$	$0.40^{+0.040}_{-0.040}$	$76.77^{+3.88}_{-4.24}$	$1.14^{+0.05}_{-0.05}$
95^{+5}_{-5}	44^{+1}_{-1}	$1.39^{+0.24}_{-0.30}$	$0.36^{+0.043}_{-0.041}$	$73.89^{+3.06}_{-3.77}$	$1.02^{+0.05}_{-0.05}$
105^{+5}_{-5}	33^{+1}_{-1}	$1.27^{+0.053}_{-0.10}$	$0.35^{+0.067}_{-0.059}$	$45.82^{+3.53}_{-4.1}$	$1.11^{+0.05}_{-0.05}$
115^{+5}_{-5}	31^{+1}_{-1}	$1.21^{+0.33}_{-0.50}$	$0.34^{+0.050}_{-0.10}$	$40.59^{+4.51}_{-4.15}$	$1.08^{+0.05}_{-0.05}$
125^{+5}_{-5}	24^{+1}_{-1}	$1.19^{+0.45}_{-0.67}$	$0.21^{+0.042}_{-0.039}$	$52.12^{+5.18}_{-3.62}$	$0.63^{+0.05}_{-0.05}$

blackbody temperature. The third panel features the total unabsorbed bolometric flux. The radius and reduced chi-square are depicted in the fourth and fifth panels. The maximum temperature (kT_{bb}) observed in the first X-ray burst is $3.05^{+0.2}_{-0.32}$ keV. However, we noticed the lower value of kT_{bb} was $\sim$1.25 keV and all other segments in all bursts kT_{bb} varied between these two values. The 11th segment of burst B4 was not a good fit, resulting in a poor chi-square of 2.7.

Table 5 Fitting results of bursts $4-6$ from observations of 4U 1323–62. Here we provide the total unabsorbed flux from $0.001-100$ keV in the unit erg $\mathrm{cm}^2\,\mathrm{s}^{-1}$.

LAXPC-10					
Burst-4					
Segment	Rate (count s^{-1})	kT_{in} (keV)	Flux $\times\ 10^{-9}$	Radius (km)	Chi-square
5^{+5}_{-5}	24^{+1}_{-1}	$1.83^{+0.08}_{-0.08}$	$0.16^{+0.033}_{-0.033}$	$45.20^{+0.82}_{-0.95}$	$1.16^{+0.05}_{-0.05}$
15^{+5}_{-5}	60^{+1}_{-1}	$2.15^{+0.18}_{-0.20}$	$0.60^{+0.048}_{-0.049}$	$87.56^{+1.19}_{-1.17}$	$1.19^{+0.05}_{-0.05}$
25^{+5}_{-5}	358^{+1}_{-1}	$2.27^{+0.05}_{-0.06}$	$3.0^{+1.17}_{-0.069}$	$96.10^{+0.32}_{-0.19}$	$1.31^{+0.05}_{-0.05}$
35^{+5}_{-5}	172^{+1}_{-1}	$2.08^{+0.08}_{-0.09}$	$1.41^{+0.064}_{-0.065}$	$94.45^{+0.35}_{-0.38}$	$1.35^{+0.05}_{-0.05}$
45^{+5}_{-5}	117^{+1}_{-1}	$1.80^{+0.09}_{-0.09}$	$1.0^{+0.095}_{-0.2}$	$90.55^{+0.45}_{-0.52}$	$0.69^{+0.05}_{-0.05}$
55^{+5}_{-5}	95^{+1}_{-1}	$1.91^{+0.13}_{-0.15}$	$0.74^{+0.049}_{-0.049}$	$90.29^{+1.15}_{-1.21}$	$1.27^{+0.05}_{-0.05}$
65^{+5}_{-5}	80^{+1}_{-1}	$1.72^{+0.15}_{-0.15}$	$0.60^{+0.044}_{-0.044}$	$88.48^{+1.09}_{-1.01}$	$1.47^{+0.05}_{-0.05}$
75^{+5}_{-5}	64^{+1}_{-1}	$1.63^{+0.16}_{-0.15}$	$0.49^{+0.042}_{-0.042}$	$86.11^{+0.79}_{-0.78}$	$1.27^{+0.05}_{-0.05}$
85^{+5}_{-5}	58^{+1}_{-1}	$1.58^{+0.15}_{-0.17}$	$0.48^{+0.042}_{-0.040}$	$86.05^{+0.75}_{-0.91}$	$1.59^{+0.05}_{-0.05}$
95^{+5}_{-5}	49^{+1}_{-1}	$2.18^{+0.30}_{-0.35}$	$0.36^{+0.042}_{-0.043}$	$79.12^{+0.52}_{-0.55}$	$1.027^{+0.05}_{-0.05}$
105^{+5}_{-5}	42^{+1}_{-1}	1.20	0.32	77.07	2.74
115^{+5}_{-5}	39^{+1}_{-1}	$1.83^{+0.39}_{-0.52}$	$0.27^{+0.036}_{-0.037}$	$71.21^{+0.32}_{-0.33}$	$1.47^{+0.05}_{-0.05}$
Burst-5					
Segment	Rate (count s^{-1})	kT_{in} (keV)	Flux $\times\ 10^{-9}$	Radius (km)	Chi-square
5^{+5}_{-5}	23^{+1}_{-1}	$0.85^{+0.052}_{-0.097}$	$0.26^{+0.051}_{-0.096}$	$39.83^{+10.12}_{-3.47}$	$1.44^{+0.05}_{-0.05}$
15^{+5}_{-5}	305^{+1}_{-1}	$2.25^{+0.069}_{-0.071}$	$2.47^{+0.087}_{-0.086}$	$94.79^{+1.66}_{-1.67}$	$1.22^{+0.05}_{-0.05}$
25^{+5}_{-5}	209^{+1}_{-1}	$2.15^{+0.082}_{-0.085}$	$1.64^{+0.073}_{-0.072}$	$99.00^{+2.26}_{-2.13}$	$1.13^{+0.05}_{-0.05}$
35^{+5}_{-5}	140^{+1}_{-1}	$2.034^{+0.11}_{-0.11}$	$1.14^{+0.060}_{-0.060}$	$90.12^{+2.47}_{-2.29}$	$1.30^{+0.05}_{-0.05}$
45^{+5}_{-5}	115^{+1}_{-1}	$1.95^{+0.13}_{-0.14}$	$0.92^{+0.074}_{-0.055}$	$87.86^{+2.74}_{-2.52}$	$1.77^{+0.05}_{-0.05}$
55^{+5}_{-5}	88^{+1}_{-1}	$1.65^{+0.13}_{-0.15}$	$0.74^{+0.049}_{-0.049}$	$85.42^{+3.02}_{-2.44}$	$1.56^{+0.05}_{-0.05}$
65^{+5}_{-5}	83^{+1}_{-1}	$1.79^{+0.16}_{-0.18}$	$0.65^{+0.048}_{-0.048}$	$83.11^{+3.23}_{-2.90}$	$1.44^{+0.05}_{-0.05}$
75^{+5}_{-5}	71^{+1}_{-1}	$2.00^{+0.18}_{-0.21}$	$0.61^{+0.049}_{-0.048}$	$81.52^{+3.46}_{-3.10}$	$0.98^{+0.05}_{-0.05}$
85^{+5}_{-5}	64^{+1}_{-1}	$1.92^{+0.27}_{-0.32}$	$0.51^{+0.047}_{-0.046}$	$77.13^{+3.73}_{-3.17}$	$1.45^{+0.05}_{-0.05}$
95^{+5}_{-5}	52^{+1}_{-1}	$1.95^{+0.27}_{-0.31}$	$0.45^{+0.046}_{-0.045}$	$74.17^{+4.02}_{-3.51}$	$0.82^{+0.05}_{-0.05}$
105^{+5}_{-5}	46^{+1}_{-1}	$1.35^{+0.34}_{-0.60}$	$0.41^{+0.041}_{-0.016}$	$56.92^{+6.96}_{-3.03}$	$1.33^{+0.05}_{-0.05}$
115^{+5}_{-5}	36^{+1}_{-1}	$2.48^{+0.74}_{-1.25}$	$0.30^{+0.19}_{-0.048}$	$58.44^{+5.21}_{-12.85}$	$0.87^{+0.05}_{-0.05}$
Burst-6					
Segment	Rate (count s^{-1})	kT_{in} (keV)	Flux $\times\ 10^{-9}$	Radius (km)	Chi-square
5^{+5}_{-5}	36^{+1}_{-1}	$2.51^{+0.17}_{-0.19}$	$0.29^{+0.10}_{-0.085}$	$64.34^{+1.04}_{-5.78}$	$1.21^{+0.05}_{-0.05}$
15^{+5}_{-5}	327^{+1}_{-1}	$2.28^{+0.069}_{-0.07}$	$2.56^{+0.088}_{-0.088}$	$95.46^{+1.72}_{-1.65}$	$1.70^{+0.05}_{-0.05}$
25^{+5}_{-5}	208^{+1}_{-1}	$2.05^{+0.075}_{-0.077}$	$1.86^{+0.072}_{-0.072}$	$94.36^{+2.1}_{-1.74}$	$1.73^{+0.05}_{-0.05}$
35^{+5}_{-5}	114^{+1}_{-1}	$1.94^{+0.11}_{-0.11}$	$1.0^{+0.07}_{-0.09}$	$88.55^{+4.33}_{-2.77}$	$0.68^{+0.05}_{-0.05}$
45^{+5}_{-5}	106^{+1}_{-1}	$1.88^{+0.12}_{-0.13}$	$0.88^{+0.051}_{-0.051}$	$88.43^{+3.26}_{-1.96}$	$1.49^{+0.05}_{-0.05}$
55^{+5}_{-5}	92^{+1}_{-1}	$1.86^{+0.16}_{-0.17}$	$0.73^{+0.049}_{-0.049}$	$86.94^{+3.07}_{0.51}$	$1.42^{+0.05}_{-0.05}$
65^{+5}_{-5}	82^{+1}_{-1}	$1.82^{+0.17}_{-0.19}$	$0.61^{+0.045}_{-0.045}$	$84.75^{+3.3}_{-2.9}$	$1.12^{+0.05}_{-0.05}$
75^{+5}_{-5}	61^{+1}_{-1}	$1.95^{+0.24}_{-0.26}$	$0.48^{+0.043}_{-0.042}$	$79.74^{+3.82}_{-0.36}$	$1.46^{+0.05}_{-0.05}$
85^{+5}_{-5}	54^{+1}_{-1}	$2.56^{+0.63}_{-0.60}$	$0.42^{+0.095}_{-0.056}$	$75.02^{+5.41}_{-7.07}$	$1.71^{+0.05}_{-0.05}$
95^{+5}_{-5}	47^{+1}_{-1}	$1.70^{+0.24}_{-0.28}$	$0.38^{+0.038}_{-0.038}$	$74.77^{+4.05}_{-3.55}$	$1.07^{+0.05}_{-0.05}$

4 DISCUSSION AND CONCLUSIONS

We present an analysis of the *AstroSat*/LAXPC observation of the NS 4U 1323–62. LAXPC's payload detected six thermonuclear X-ray bursts and two dips from the source. Each burst had similar wait times between consecutive bursts except for the gap observed between the bursts B3–B4 and B5–B6, which is nearly double the wait time of consecutive bursts. We produced linear and quadratic orbital ephemerides to find the value of the orbital period is $\sim$2.65 to 2.70 h, This is compatible with previous estimations, as displayed in Table 1.

The large effective area of LAXPC's detector allowed us to generate the energy resolved burst profile at a higher energy band. We found that bursts were detected up to 20 keV. Above 20 keV, the LAXPC instruments showed negligible count rate in the light curve of 4U 1323–62. However, the hard X-ray light curves during the bursts were found to be consistent with the pre-burst emission. We observed strong energy dependence of burst decay times. The increase in energy along with decreasing burst decay time suggest the cooling of burning ashes (Galloway & Keek 2017a).

LFQPOs are observed in the PDS of the accreting NSs, non-pulsating NSs and from BH binaries. The phenomenon of QPO frequency ($0.6-2.4$ Hz) for atoll sources depends on the photon energy. The observed QPO frequency $\sim$1 Hz signifies a high-inclination system (Homan et al. 2015). The occurrence of QPOs is due to the physical and geometric change in the accretion disk. The disturbance of the inner accretion disk is the reason for the emission matter from the boundary layer or the surface of the NS.

The state of the source was estimated by the normalization of components, which was highly variable during the bursts. During the soft state, emission was from the accretion disc, and the harder one was from the boundary layer. Applying our model, we investigated constraints that can be obtained from data with much higher statistical precision than presently available. The burst spectrum is described in the energy band $3.0 - 20.0$ keV reasonably well by either a blackbody or power law component. Time resolved spectroscopy of the thermonuclear bursts indicated that the blackbody temperature varies from $\sim$3.0 to $\sim$1.0 as the bursts progress. The bolometric unabsorbed flux is found to decrease monotonically with blackbody temperature during the thermonuclear bursts. To average all the values of flux, the mean flux for 4U 1323–62 was obtained, i.e., $\sim 1.80\times10^{-9}$ erg cm^2 s^{-1}.

We also performed time-resolved spectroscopy of the burst utilizing the standard technique. The evolution of temperature and radius indicates the Photosphere Radius Expansion (PRE). The rising phase of the bursts suggested that the emission during a burst reached its highest limit, while the persistent emission was at the lowest limit. A large increase in the burst flux during the rising phase was ascertained in very few NS LMXB systems such as GRS 1741.9–2853 and MXB 1658-298. Our analysis showed that the radius expansion phase persists for $10-30$ s, which was slowly increasing as compared to the increase in radius in other LMXB systems like 4U 1608–52 and 4U 1728–34 (Zhang et al. 2016).

The radius of the blackbody was highly consistent with the flux of each segment of the bursts. We extracted the apparent radius between $\sim$96 km – $\sim$40 km, under the assumption of an isotropically emitting spherical surface at a distance of 10 kpc. In our observations, it had been noticed that the flux continues to increase considering the maximum radius of the blackbody, such that total flux is strongly correlated with the radius.

Acknowledgements We acknowledge support from the Indian Space Research Organization (ISRO) and *AstroSat* science support cell in various aspects of instrument building, testing, software development and mission operation during the payload verification phase. We thank the LAXPC instrument team. JR wishes to thank IUCAA for research facilities.

References

Agrawal, P. C. 2006, Advances in Space Research, 38, 2989

Agrawal, P. C., Yadav, J. S., Antia, H. M., et al. 2017, A&A, 38, 30

Antia, H. M., Yadav, J. S., Agrawal, P. C., et al. 2017, ApJS, 231, 10

Arnaud, K. A. 1996, in ASPC Series, 101, Astronomical Data Analysis Software and Systems V, eds. Jacoby, G. H., & Barnes, J., 17

Ballantyne, D. R., & Everett, J. E. 2005, ApJ, 626, 364

Ballantyne, D. R., & Strohmayer, T. E. 2004, ApJ, 602, L105

Balman, Ş. 2010, MNRAS, 407, 1895

Balucińska-Church, M., Barnard, R., Church, M. J., & Smale, A. P. 2001, A&A, 378, 847

Bałucińska-Church, M., Church, M. J., Oosterbroek, T., et al. 1999, A&A, 349, 495

Bałucińska-Church, M., Dotani, T., Hirotsu, T., & Church, M. J. 2009, A&A, 500, 873

Barnard, R., Balucińska-Church, M., Smale, A. P., & Church, M. J. 2001, A&A, 380, 494

Barret, D., Olive, J.-F., & Miller, M. C. 2005, MNRAS, 361, 855

Belian, R. D., Conner, J. P., & Evans, W. D. 1976, in BAAS, 8, 442

Belloni, T. M., & Stella, L. 2014, Space Sci. Rev., 183, 43

Beri, A., Paul, B., Yadav, J. S., et al. 2019, MNRAS, 482, 4397

Bhattacharyya, S., Yadav, J. S., Sridhar, N., et al. 2018, ApJ, 860, 88

Bhulla, Y., Misra, R., Yadav, J. S., & Jaaffrey, S. N. A. 2019, RAA (Research in Astronomy and Astrophysics), 19, 114

Bildsten, L. 1998, in The Many Faces of Neutron Stars, eds. R. Buccheri, J. van Paradijs, & A. Alpar, 515, 419 (Boston: Kulwer Academic Publishers)

Boirin, L., Méndez, M., Díaz Trigo, M., Parmar, A., & Kaastra, J. 2005, in SF2A-2005: Semaine de l'Astrophysique Francaise, eds. F. Casoli, T. Contini, J. M. Hameury, & L. Pagani, 443

Boutloukos, S., Miller, M. C., & Lamb, F. K. 2010, ApJ, 720, L15

Chauhan, J. V., Yadav, J. S., Misra, R., et al. 2017, ApJ, 841, 41

Church, M. J., Gibiec, A., & Bałucińska-Church, M. 2014, MNRAS, 438, 2784

Church, M. J., Inogamov, N. A., & Bałucińska-Church, M. 2002, A&A, 390, 139

Church, M. J., Reed, D., Dotani, T., Bałucińska-Church, M., & Smale, A. P. 2005, MNRAS, 359, 1336

Degenaar, N., Koljonen, K. I. I., Chakrabarty, D., et al. 2016, MNRAS, 456, 4256

Degenaar, N., Ballantyne, D. R., Belloni, T., et al. 2018, Space Sci. Rev., 214, 15

Done, C., Gierliński, M., & Kubota, A. 2007, A&A Rev., 15, 1

Forman, W., Jones, C., Cominsky, L., et al. 1978, ApJS, 38, 357

Frank, J. 1987, Science, 236, 1007

Galloway, D. K., Chakrabarty, D., Cumming, A., et al. 2004, in AIPC Series, 714, X-ray Timing 2003: Rossi and Beyond, eds. P. Kaaret, F. K. Lamb, & J. H. Swank, 266

Galloway, D. K., Chakrabarty, D., Muno, M. P., & Hartman, J. M. 2003, in Bulletin of the American Astronomical Society, 35, AAS/High Energy Astrophysics Division #7, 864

Galloway, D. K., & Keek, L. 2017a, arXiv:1712.06227

Galloway, D. K., & Keek, L. 2017b, arXiv:1712.06227

Galloway, D. K., Muno, M. P., Hartman, J. M., Psaltis, D., & Chakrabarty, D. 2008, ApJS, 179, 360

Gambino, A. F., Iaria, R., Di Salvo, T., et al. 2016, A&A, 589, A34

Gilfanov, M., Revnivtsev, M., & Molkov, S. 2003a, A&A, 410, 217

Gilfanov, M., Revnivtsev, M., & Molkov, S. 2003b, A&A, 410, 217

Grindlay, J., Gursky, H., Schnopper, H., et al. 1976, ApJ, 205, L127

Hanawa, T. 1989, ApJ, 341, 948

Hansen, C. J., & van Horn, H. M. 1975, ApJ, 195, 735

Hasinger, G., & van der Klis, M. 1989, A&A, 225, 79

Homan, J., Buxton, M., Markoff, S., et al. 2005, ApJ, 624, 295

Homan, J., Fridriksson, J. K., & Remillard, R. A. 2015, ApJ, 812, 80

Homan, J., Jonker, P. G., Wijnands, R., van der Klis, M., & van Paradijs, J. 1999, ApJ, 516, L91

Ingram, A., & Done, C. 2011, MNRAS, 415, 2323

Jonker, P. G., van der Klis, M., & Wijnands, R. 1999, ApJ, 511, L41

Keek, L., Ballantyne, D., Kuulkers, E., & Strohmayer, T. 2014a, in The X-ray Universe 2014, 97

Keek, L., Ballantyne, D. R., Kuulkers, E., & Strohmayer, T. E. 2014b, ApJ, 797, L23

Keek, L., Galloway, D. K., in't Zand, J. J. M., & Heger, A. 2010, ApJ, 718, 292

Krimm, H. A., Holland, S. T., Corbet, R. H. D., et al. 2013, ApJS, 209, 14

Lamb, D. Q., & Lamb, F. K. 1978, ApJ, 220, 291

Lewin, W. H. G., & van den Heuvel, E. P. J. 1984, Science, 225, 1143

Lewin, W. H. G., van Paradijs, J., & Taam, R. E. 1993, Space Sci. Rev., 62, 223

Linares, M., Watts, A., Altamirano, D., et al. 2009, The Astronomer's Telegram, 1979

Maraschi, L., & Cavaliere, A. 1977, in X-ray Binaries and Compact Objects, ed. K. A. van der Hucht, 127

Méndez, M. 2000, Nuclear Physics B Proceedings Supplements, 80, 15

Méndez, M., & van der Klis, M. 1999, ApJ, 517, L51

Méndez, M., van der Klis, M., & Ford, E. C. 2001, ApJ, 561, 1016

Mitsuda, K., Inoue, H., Koyama, K., et al. 1984, PASJ, 36, 741

Mondal, A. S., Dewangan, G. C., Pahari, M., & Raychaudhuri, B. 2018, MNRAS, 474, 2064

Motta, S. E. 2016, Astronomische Nachrichten, 337, 398

Noble, M. S., & Nowak, M. A. 2008, PASP, 120, 821

Parmar, A. N., Gottwald, M., van der Klis, M., & van Paradijs, J. 1989, ApJ, 338, 1024

Paul, B. 2013, International Journal of Modern Physics D, 22, 1341009

Popham, R., & Sunyaev, R. 2001, X-ray Astronomy: Stellar Endpoints, AGN, and the Diffuse X-ray Background, 599, 870

Reig, P. 2011, Ap&SS, 332, 1

Roy, J., Agrawal, P. C., Dedhia, D. K., et al. 2016, Experimental Astronomy, 42, 249

Scaringi, S. 2015, Acta Polytechnica CTU Proceedings, 2, 107

Strohmayer, T., & Bildsten, L. 2006, New Views of Thermonuclear Bursts, eds. W. H. G. Lewin, & M. van der Klis, Compact Stellar X-ray Sources, 113

Swank, J. H., Becker, R. H., Boldt, E. A., et al. 1977, ApJ, 212, L73

Tawara, Y., Hirano, T., Kii, T., Matsuoka, M., & Murakami, T. 1984, PASJ, 36, 861

Ubertini, P., Bazzano, A., Cocchi, M., et al. 1999, ApJ, 514, L27

Urpin, V., Konenkov, D., & Geppert, U. 1998, MNRAS, 299, 73

van der Klis, M. 2000, ARA&A, 38, 717

van der Klis, M. 2006, Rapid X-ray Variability, eds. W. H. G. Lewin, & M. van der Klis, Compact Stellar X-ray Sources, 39

van der Klis, M., Parmar, A., van Paradijs, J., et al. 1985, IAU Circ., 4044

Wang, J. 2016, International Journal of Astronomy and Astrophysics, 6, 82

Warwick, R. S., Marshall, N., Fraser, G. W., et al. 1981, MNRAS, 197, 865

Woosley, S. E., & Taam, R. E. 1976, Nature, 263, 101

Yadav, J. S., Misra, R., Verdhan Chauhan, J., et al. 2016a, ApJ, 833, 27

Yadav, J. S., Agrawal, P. C., Antia, H. M., et al. 2016b, in Proc. SPIE, 9905, Space Telescopes and Instrumentation 2016: Ultraviolet to Gamma Ray, 99051D

Zhang, G., Méndez, M., & Altamirano, D. 2011, MNRAS, 413, 1913

Zhang, G., Méndez, M., Zamfir, M., & Cumming, A. 2016, MNRAS, 455, 2004